scientific reports

Check for updates

OPEN

Resting state BOLD-perfusion coupling patterns using multiband multi-echo pseudo-continuous arterial spin label imaging

Alexander D. Cohen[1]✉, Stefano Moia[2,3], G. Bruce Pike[4], César Caballero-Gaudes[5,6] & Yang Wang[1]

The alteration of neurovascular coupling (NVC), where acute localized blood flow increases following neural activity, plays a key role in several neurovascular processes including aging and neurodegeneration. While not equivalent to NVC, the coupling between simultaneously measured cerebral blood flow (CBF) with arterial spin labeling (ASL) and blood oxygenation dependent (BOLD) signals, can also be affected. Moreover, the acquisition of BOLD data allows the assessment of resting state (RS) fMRI metrics. In this study a multiband, multi-echo (MBME) pseudo-continuous ASL (pCASL) sequence was used to collect simultaneous BOLD and ASL data in a group of healthy control subjects, and the patterns of BOLD-CBF coupling were evaluated. Coupling was also correlated with the BOLD RS measures. The variability, reproducibility, and reliability of the metrics were also computed in a multi-session subgroup. Areas of higher coupling were observed in the visual, motor, parietal, and frontal cortices and corresponded to major brain networks. Areas of significant correlation between coupling and BOLD RS measures corresponded to areas of heightened coupling. Higher variability and lower reliability were found for coupling metrics compared to BOLD RS metrics. These results indicate BOLD-CBF coupling metrics may be useful for studying neurovascular physiology.

Keywords Arterial spin labeling, BOLD, Multiband, Multi-echo, BOLD-CBF coupling

Neurovascular coupling (NVC) is vital for cerebral homeostasis[1,2]. NVC, where acute localized blood flow is altered following neural activity, is the basis for the Blood Oxygenation Level-Dependent (BOLD) response in functional magnetic resonance imaging (fMRI)[3]. In this process, neural activity results in increased oxygen demand leading to increased blood flow and oxygen supply to that region. Since the increased oxygen supply is typically more than the cerebral metabolic rate of oxygenation [$CMRO_2$]) the oxygenated to deoxygenated hemoglobin ratio is increased. Since oxygenated hemoglobin has lower magnetic susceptibility compared to deoxygenated hemoglobin, the magnetic resonance signal increases in that region. Emerging research suggests that impaired NVC plays a critical role in several neurovascular pathological processes. For example, research has shown NVC is a factor in cognitive decline in aging and neurodegeneration[4] and suggests that neurovascular uncoupling is associated with microvascular pathophysiological alterations and has a causal role in developing Alzheimer's Disease (AD) and AD-related cognitive decline[4–7].

Arterial spin labeling (ASL), a non-invasive MRI technique used to measure CBF, and blood oxygenation dependent (BOLD) contrasts can be collected simultaneously using single shot multi-echo sequences[8–12]. Using these sequences, the correlation between the ASL and BOLD time series (BOLD-CBF coupling) can be directly calculated. While not equivalent to NVC, BOLD-CBF coupling can provide insight into brain physiology[10,11,13,14]. For example, Tak et al. showed the degree of positive BOLD-CBF coupling decreased with the brain microvasculature fraction[11] and positively correlated with resting state functional connectivity (RSFC) within functional networks[10]. Champagne et al. showed BOLD-CBF coupling played a significant role in RSFC strength differences between young and old participants while other measures such as baseline CBF

[1]Department of Radiology, Medical College of Wisconsin, 8701 Watertown Plank Road, Milwaukee, WI 53226, USA. [2]Neuro-X Institute, École polytechnique fédérale de Lausanne, Geneva, Switzerland. [3]Department of Radiology and Medical Informatics (DRIM), Faculty of Medicine, University of Geneva, Geneva, Switzerland. [4]Departments of Radiology and Clinical Neurosciences, and Hotchkiss Brain Institute, University of Calgary, Calgary, Canada. [5]Basque Center on Cognition, Brain and Language, San Sebastián – Donostia, Spain. [6]Ikerbasque, Basque Foundation for Science, Bilbao, Spain. ✉email: acohen@mcw.edu

and cerebrovascular reactivity (CVR) did not show such an effect[15]. In addition, these sequences allow calibrated fMRI, which separates oxygen metabolism changes from blood flow and volume changes, to be performed using the Davis model[16].

Furthermore, resting state fluctuation metrics quantify the characteristics of spontaneous brain fluctuations. For example, the amplitude of low-frequency fluctuations (ALFF) metric calculates the power of low-frequency oscillations in the BOLD signal[17]. These low-frequency signals are usually the basis of RSFC[18]. ALFF and RSFC provide complementary information, with ALFF measuring local neural activity and RSFC measuring long-range brain connections. For example, higher ALFF values have been associated with stronger network connectivity in several brain networks[19]. ALFF has also allowed differentiating between physiological states[20]. For instance, ALFF was significantly increased for an eyes open vs. eyes closed task in the visual cortex[20]. One study also evaluated the coupling of CBF and ALFF showing that the metrics are indeed significantly coupled, and showed regional changes in CBF-ALFF coupling with age while also being affected by sex and executive function[21].

Regional homogeneity (ReHo) is another common resting state metric that describes the temporal coherence of the signal in a voxel with the voxel's neighbors[22,23]. It has been shown to be related to ALFF[24]. In addition, CBF-ReHo correlations and the CBF/ReHo ratio have been found altered in disease[25,26]. Similar to ALFF, ReHo and RSFC provide complementary information with ReHo measuring local synchronization of brain activity. However, one study found changes in ReHo were associated with changes in RSFC[27].

While most studies on BOLD-CBF coupling use a dual-echo approach, with a short echo time (~10ms) to obtain a perfusion-weighted signal, and a longer echo time (~30ms) for T2*-weighted BOLD contrasts, Cohen and colleagues combined a multiband acquisition with four echoes[28]. The collection of multiple echoes allowed data denoising with multi-echo independent component analysis (ME-ICA)[29–35]. This technique classifies spatially independent components as either BOLD or non-BOLD based on whether or not their amplitudes are linearly dependent on TE, respectively. The non-BOLD components can then be removed from the data via nuisance regression or treated as regressors of non-interest in task analysis[36]. Using this multiband, multi-echo (MBME) pCASL/BOLD sequence, they found BOLD-CBF coupling strength was higher and the area of significant coupling was larger for the denoised multi-echo combined data compared to multi-echo combined data without ME-ICA denoising[28].

Although there have been a limited number of studies investigating BOLD-CBF coupling, especially with MBME pCASL/BOLD sequences[28], the reproducibility of BOLD-CBF coupling metrics, in particular, has not been studied. The relationship between BOLD-CBF coupling and traditional RSFC metrics, including ReHo and ALFF, is also unknown. Therefore, in this study resting state fMRI data was collected using a MBME pCASL/BOLD sequence with four echoes in a group of healthy volunteers. Building on previous research investigating the relationship between BOLD-CBF coupling and RSFC, here BOLD-CBF coupling metrics were computed and then correlated with ReHo and ALFF. A subset of subjects returned within two weeks for a repeat scan to assess the variability, reproducibility, and reliability of these measures.

Materials and methods

Subjects

This study was approved by the Medical College of Wisconsin Institutional Review Board and was conducted in accordance with the Declaration of Helsinki. All subjects provided written informed consent prior to participation in this study. In total, 28 healthy volunteer subjects (Mean Age = 28.0 y.o., Range 20–46 y.o., 9 Male, 19 Female) participated in this study. Of those, 19 subjects returned (Mean Age = 27.2 y.o., Range 20–46 y.o., 7 Male, 12 Female) within two weeks to repeat the study resulting in 47 imaging sessions. Subjects were instructed to refrain from caffeine and tobacco for six hours prior to imaging.

Imaging

Imaging was performed on a 3T scanner (Signa Premier, GE Healthcare, Waukesha, WI) with a body transmit coil and a 32-channel NOVA (Nova Medical, Wilmington, MA) receive head coil. Maximum gradient strength was 70mT/m and the maximum slew rate was 170 mT/m/ms. A 3D T1-weighted MPRAGE anatomical image was acquired with TR/TE = 2200/2.8ms, FOV = 24 cm, matrix size = 240 × 240 × 128, slice thickness = 1.0 mm, voxel size = 1 × 1 × 1 mm^3 zero-filled to 512 × 512 × 256, and FA = 8°. Each subject underwent a MBME simultaneous pCASL/BOLD resting state fMRI acquisition (Cohen et al., 2017; Cohen et al., 2018) with the following parameters: TR/TE = 3500/11,30,49,67ms, FOV = 24 cm, matrix size = 80 × 80 with slice thickness = 3 mm (3 × 3 × 3 mm voxel size), 11 excitations with multiband factor = 4 (i.e. 44 total slices in total), FA = 90°, partial Fourier factor = 0.85, effective echo spacing = 0.25ms, readout length = 20.0ms. Fat suppression was used. The sequence also incorporated an unbalanced pCASL labeling scheme with labeling time = 1.5s and PLD = 1.0s. Resting state scans used a single shot EPI readout with in-plane acceleration (R) = 2 and lasted six minutes resulting in 103 volumes. During the resting state scans, subjects were instructed to close their eyes, but remain awake, refrain from any motion, and not think about anything in particular.

Analysis

A combination of Freesurfer[37], AFNI[38,39], FSL[40], and Matlab (The Mathworks, R2018a) were used for the data analysis. Image preprocessing was conducted based on the HCP minimal preprocessing pipeline modified to take into account the multiple echoes[41].

Anatomical processing

Anatomical processing used the *PreFreeSurferPipeline.sh* scripts from the HCP pipeline. First, the anatomical image was aligned to the anterior-posterior commissure line (ACPC) using *aff2rigid* in FSL. Next, a brain mask

was created using FNIRT-based brain extraction. This process involved first linearly registering the MPRAGE image to MNI space using *flirt* in FSL with 12 degrees of freedom[42], then non-linearly refining the registration with *fnirt* in FSL. Finally, a brain-only reference image in MNI space was inverse warped to native space using the transformations determined above and used to mask the MPRAGE image to extract the brain. This MPRAGE brain-only image was then registered to MNI space using *flirt* with 12 degrees of freedom followed by *fnirt*.

In addition, a FreeSurfer analysis was performed for all subjects using the *recon-all* command on the ACPC-aligned MPRAGE dataset. The purpose was to extract individual brain parcellations to use for the ROI-based analyses described below.

BOLD preprocessing

The first four volumes were discarded to allow the signal to reach a steady-state magnetization. Next, the data was volume registered to the first volume using *mcflirt* in FSL. Of note, only the first echo was volume registered, and subsequent echoes were volume registered using the transformation matrices from the first echo.

Then, ME-ICA was performed using *tedana v0.0.11* (https://zenodo.org/record/5541689). A user-defined mask, generated using *3dAutomask* in AFNI, was applied to the data. An adaptive mask was then generated, in which each voxel's value reflects the number of echoes with 'good' data. A two-stage masking procedure was applied, in which a liberal mask (including voxels with good data in at least the first echo) was used for optimal combination, T2*/S0 estimation, and denoising, while a more conservative mask (restricted to voxels with good data in at least the first three echoes) was used for the component classification procedure. A monoexponential model was fit to the data at each voxel using log-linear regression in order to estimate T2* and S0 maps. Multi-echo data were then optimally combined using the T2* combination method[43]. Principal component analysis (PCA) based on the PCA component estimation with a Moving Average (stationary Gaussian) process[44] was then applied to the optimally combined data for dimensionality reduction, where the number of components was chosen according to the MDL criterion. Independent component analysis was then used to decompose the dimensionally reduced dataset with an equal number of spatially independent components. Next, component selection was performed to identify BOLD, non-BOLD, and uncertain (low-variance) components using the Kundu decision tree v2.5[34], with manual supervision of the automatic results. The accepted and uncertain components were then retained, while the rejected components were removed from the timeseries by the means of aggressive nuisance regression. No additional motion correction was performed as ICA models have been shown to reduce motion-related effects in the signal[36]. Importantly, for all cases, a perfusion-weighted component was identified and regressed from the data. Finally, the denoised data was bandpass filtered with $0.01 < f < 0.071$ Hz corresponding to 1/(4*TR).

ASL preprocessing

The perfusion-weighted signal was also denoised following a similar procedure as presented in Cohen et al.[14]. The following algorithm was applied to the first-echo data *prior* to highpass filtering and demodulation. First, all components identified by the BOLD ME-ICA procedure in were correlated with a timeseries of alternating 0's and 1's to identify components associated with the label-control oscillations. To avoid removing perfusion-weighted (PW) signal, components with Pearson's correlation $(r) > 0.2$ were not regressed. All other components, including the both accepted and rejected components from the ME-ICA performed in Sect. 2.3.2, were regressed from the first-echo data using *tedana*. A denoised PW timeseries was generated by highpass filtering at $f > 1/(4*TR)$ and demodulating the denoised first echo signal[45]. To examine the effect of the PW denoising, temporal SNR (tSNR) was computed for the denoised and non-denoised PW timeseries by dividing the mean by the standard deviation of the signal.

BOLD-CBF coupling

The BOLD-CBF coupling was assessed by correlating the signals from the denoised BOLD and PW datasets on a voxelwise basis using Pearson correlation with *3dTcorrelate* in AFNI. Following the procedures outlined in Tak and colleagues[11], the BOLD time series was time-shifted from −2TR to +2TR (-7.0–7.0s) with steps of 1 TR. The voxelwise maximum correlation within this range was defined as r_{max}. The correlation at zero time shift (r_0) was also extracted. Correlation maps were converted to z-scores using a Fisher's z transform. A one sample t-test was run on the coupling metrics to identify group patterns using *3dttest++* in AFNI. Maps were thresholded at $p < 0.001$ and then cluster-size corrected for multiple comparisons at $\alpha < 0.05$ using *3dClustSim* in AFNI. In addition, mean values for each metric were extracted from ROIs consisting of the Yeo 7 network template[46]. Networks corresponded to: Yeo1 = Visual; Yeo2 = Somatomotor; Yeo3 = Dorsal Attention; Yeo4 = Ventral Attention; Yeo5 = Limbic; Yeo6 = Frontoparietal; Yeo7 = Default Mode.

In addition, a whole-GM ROI-based coupling analysis was conducted using ROIs derived from the parcellations estimated by FreeSurfer on individual brains. For each subject, FreeSurfer parcellated the brain cortex into 148 ROIs. In addition, 16 subcortical ROIs from the same parcellation were included in the analysis. The average BOLD signal from each of these ROIs for each subject and timepoint was correlated with the average PW signal from the same ROI and all other ROIs. The same time shift analysis was performed as for the voxelwise analysis and r_{max} and r_0 were computed. This resulted in 164×164 r_{max} and r_0 BOLD-CBF coupling matrices for each timepoint and subject. These coupling matrices were then averaged across subjects. This ROI-based coupling analysis was carried out using custom code written in Matlab.

Traditional RS metrics

ALFF was computed using *3dRSFC* in AFNI with $0.01 < f < 0.071$ Hz and ReHo using *3dReHo* in AFNI with a 27 voxel neighborhood. ALFF and ReHo were computed for both BOLD and PW data. ALFF and ReHo were normalized by dividing each voxel by the whole-brain mean value (mALFF and mReHo respectively) to allow

for comparisons across subjects. Voxelwise group-averaged mALFF and mReHo were computed across subjects. Mean values for mALFF and mReHo were also extracted from ROIs consisting of the Yeo 7 network template[46].

Correlation of coupling with traditional RS metrics
To examine the relationship between BOLD-CBF Coupling and the traditional RS metrics, r_{max} and r_0 were correlated with mALFF and mReHo on a voxelwise basis across subjects using *3dTcorrelate* in AFNI with Pearson correlation. The resulting correlation maps were thresholded at $p < 0.05$ and then cluster-size corrected for multiple comparisons at $\alpha < 0.05$ using *3dClustSim* in AFNI.

Variability, reproducibility and reliability analyses
For the 19 subjects with repeat datasets the variability of coupling and mALFF and mReHo was estimated using within the subject standard deviation (wSD) and between subject standard deviation (bSD). wSD was estimated using Eq. (1) where N is the number of subjects and $x_{i1} - x_{i2}$ is the difference in metric x (i.e. r_{max}, r_0, etc.) between the two time points (TPs). bSD was computed by averaging each metric across the two TPs and then computing the standard deviation across subjects.

$$wSD = \sqrt{\frac{1}{2N}\sum (x_{i1} - x_{i2})^2} \tag{1}$$

In addition, reproducibility was estimated using Eq. (2)[47,48]. Here x_{i1} and x_{i2} are the values of each metric at TP1 and TP2 respectively. If values are ≥ 0, Rep ranges from 0 to 1 with higher values being desirable. If the difference between two values is large, Rep approaches 0. This metric controls for large outliers in the data but can blow up if there are negative values as the numerator becomes large, and the denominator becomes small. Variability and reproducibility metrics were computed using the mean values extracted from the Yeo 7 network ROIs.

$$Rep = 1 - \left|\left(\frac{x_{i1} - x_{i2}}{x_{i1} + x_{i2}}\right)\right|$$

Finally, reliability was estimated using ICC(2,1) on a voxelwise basis using *3dICC* in AFNI.

Surface projection
Surface images were created in gifti format and viewed using the Human Connectome Project (HCP) workbench software v 1.5.0 (*wb_view)* by projecting the volume images to an inflated template gifti surface.

Results

ASL TSNR results

tSNR was compared between the denoised and non-denoised PW signal. Results are shown in Fig. 1. Qualitatively, tSNR was higher for the denoised PW data compared to non-denoised data. This is confirmed by the paired t-test which shows widespread higher TSNR for the denoised data.

BOLD-CBF coupling

Individual subject and group-averaged BOLD-CBF coupling results are shown for r_0 and r_{max} in Fig. 2a and b respectively for a representative subject (left) and the group average (middle). For r_0 heightened coupling was observed in the visual cortex, parietal areas, frontal regions, and motor cortices. For r_{max}, heightened coupling was more widespread, with coupling highest in the visual cortex and parietal regions.

One sample t-test results for the r_0 and r_{max} are also shown in Fig. 2 (right). Maps were thresholded at a high t-score ($t > 4$). Despite this, for r_{max}, nearly the entire brain was significant. For r_0 only the temporal lobe, subcortex, and orbitofrontal cortex (OFC) were not significant.

Results of the ROI-based BOLD-CBF coupling analysis are shown in Fig. 3. BOLD-CBF coupling matrices for r_{max} and r_0 were qualitatively similar. BOLD-CBF coupling matrices for TP1 and TP2 were also qualitatively similar. A prominent diagonal line of higher correlation is present for all matrices indicating a higher correlation between BOLD and PW timeseries of the same ROI compared to other ROIs. Secondary diagonals are observed in the bottom left and top right of the matrices. These correspond to the analogous contralateral ROIs. The first 16 ROIs are the subcortical ROIs. BOLD and PW timeseries extracted from subcortical ROIs were more closely correlated with other subcortical ROIs compared to cortical ROIs.

Traditional RS metrics

Group averaged traditional RSFC metrics, including mALFF and mReHo, are shown in Fig. 4. Qualitatively, BOLD and ASL mReHo and mALFF were very similar.

Quantitative results

Quantitative results for the BOLD-CBF coupling and traditional RS metrics are shown in Fig. 5 (top) and Fig. 5 (bottom) respectively. Mean values were extracted from the 7 Yeo functional networks for TP1 and TP2 separately. For all metrics there was no significant difference between TP1 and TP2 for any ROI. Values of r_0 and r_{max} were slightly variable across ROIs, especially for Yeo5. This ROI, corresponding to the limbic system, had the lowest r_0 and r_{max} of all ROIs. Similar results were seen for mALFF and mReHo with Yeo5 showing the lowest values.

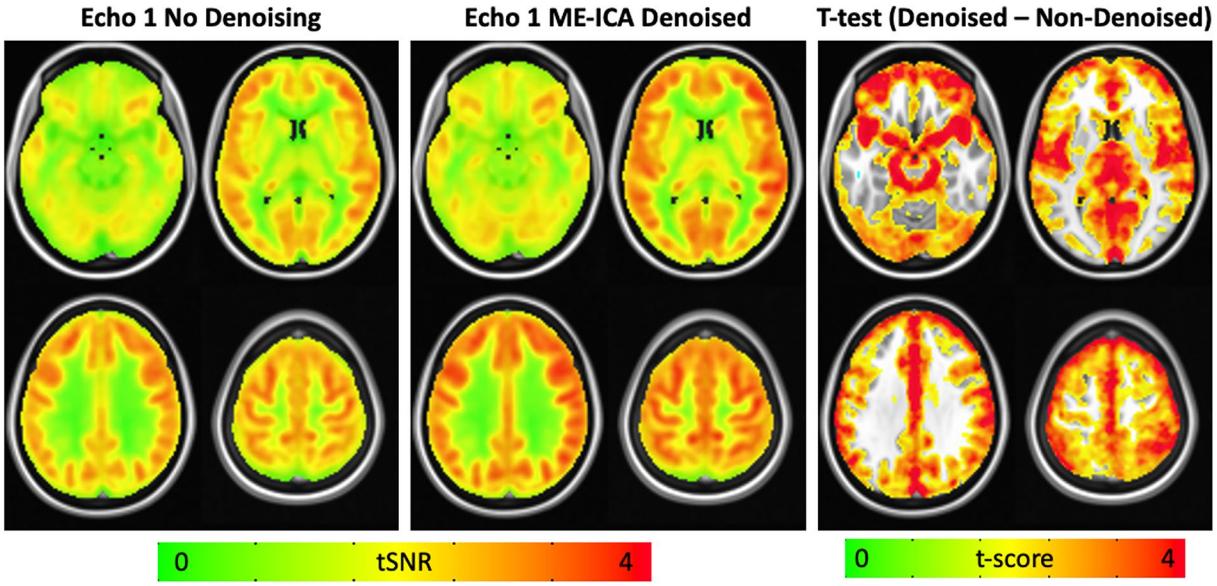

Fig. 1. Perfusion-weighted signal tSNR for non-denoised and ME-ICA denoised datasets. Qualitatively, tSNR was higher for the denoised PW data compared to non-denoised data. This is confirmed by the paired t-test which shows widespread higher tSNR for the denoised data. The t-score maps were thresholded at $p < 0.001$. No negative values were observed.

Correlation of coupling with RS Metrics

Figure 6 shows the results of the correlation between BOLD-CBF coupling metrics (r_0 and r_{max}) and traditional resting state metrics (mALFF and mReHo). Overall, results for r_0 and r_{max} were similar for all RS metrics. BOLD-CBF coupling and mALFF were significantly correlated mainly in the visual cortex and motor cortex. Some significant correlation between BOLD-CBF coupling and mALFF was also seen in parietal and frontal areas. Significant correlation between BOLD-CBF coupling and mReHo was also seen in the visual cortex, motor cortex, parietal areas, and, to a lesser extent, frontal areas.

Variability, reproducibility, and reliability

Results for wSD, bSD, and Reproducibility are shown in Table 1 for BOLD-CBF coupling metrics and in Table 2 for RS metrics. In general, reproducibility was higher for RS metrics compared to coupling metrics with values greater than 0.95 for all RS metrics across networks. For coupling metrics, reproducibility was higher for r_{max} compared to r_0 with values consistently greater than 0.9 across ROIs. Surprisingly, wSD was higher than bSD for more than half of ROIs for the BOLD-CBF coupling metrics but was lower than bSD for the majority of ROIs for mALFF and mReHo.

Reliability was measured on a voxelwise basis using ICC(2,1). Results are shown in Fig. 7. In general, ICC was higher for the RS metrics compared to BOLD-CBF coupling metrics. mALFF had the highest ICC with values consistently greater than 0.8 across the cortex. ICC was lower for ASL mReHo than for BOLD mReHo. In general, ICC was low for the BOLD-CBF coupling metrics, although areas with higher ICC were seen in the visual and motor cortices. These areas corresponded to areas of higher correlation between BOLD-CBF coupling metrics and RS metrics (see Fig. 6).

Discussion

In this study patterns of the correlation of BOLD and ASL time series, or BOLD-CBF coupling, were characterized using an MBME PCASL/BOLD sequence to simultaneously measure BOLD and PW signals. Multi-echo ICA was then used to denoise the BOLD and PW signals. Areas of greatest coupling were observed in the visual, motor, parietal, and frontal cortices. The main findings of this study were two-fold: First, BOLD-CBF coupling metrics (r_0 and r_{max}) were widespread and significantly correlated with traditional RS metrics including mReHo and mALFF, with areas of significant correlation corresponding to areas of high coupling. Second, the reproducibility and reliability of BOLD-CBF coupling metrics was evaluated and showed higher variability of coupling metrics compared to RS metrics. Reliability, measured using ICC, was also lower for coupling metrics with areas of higher ICC corresponding to areas of heightened coupling.

Overall, widespread coupling was observed between BOLD and PW time series. In general, t-test results showed more widespread BOLD-CBF coupling compared to previous studies. This was likely driven by ME-ICA denoising made possible by the MBME BOLD/ASL sequence. Instead of the typical dual-echo sequences, four echoes were used in this study. For example, Tak et al. showed significant BOLD/PW coupling in well-known resting state networks including the default mode, visual, and task-positive networks at uncorrected $p < 0.005$ [11]. Another study found more widespread significant coupling in young adults in similar regions with stronger coupling in medial, parietal, and frontal areas with FDR corrected $p < 0.05$ [13]. In the present study, for both r_{max}

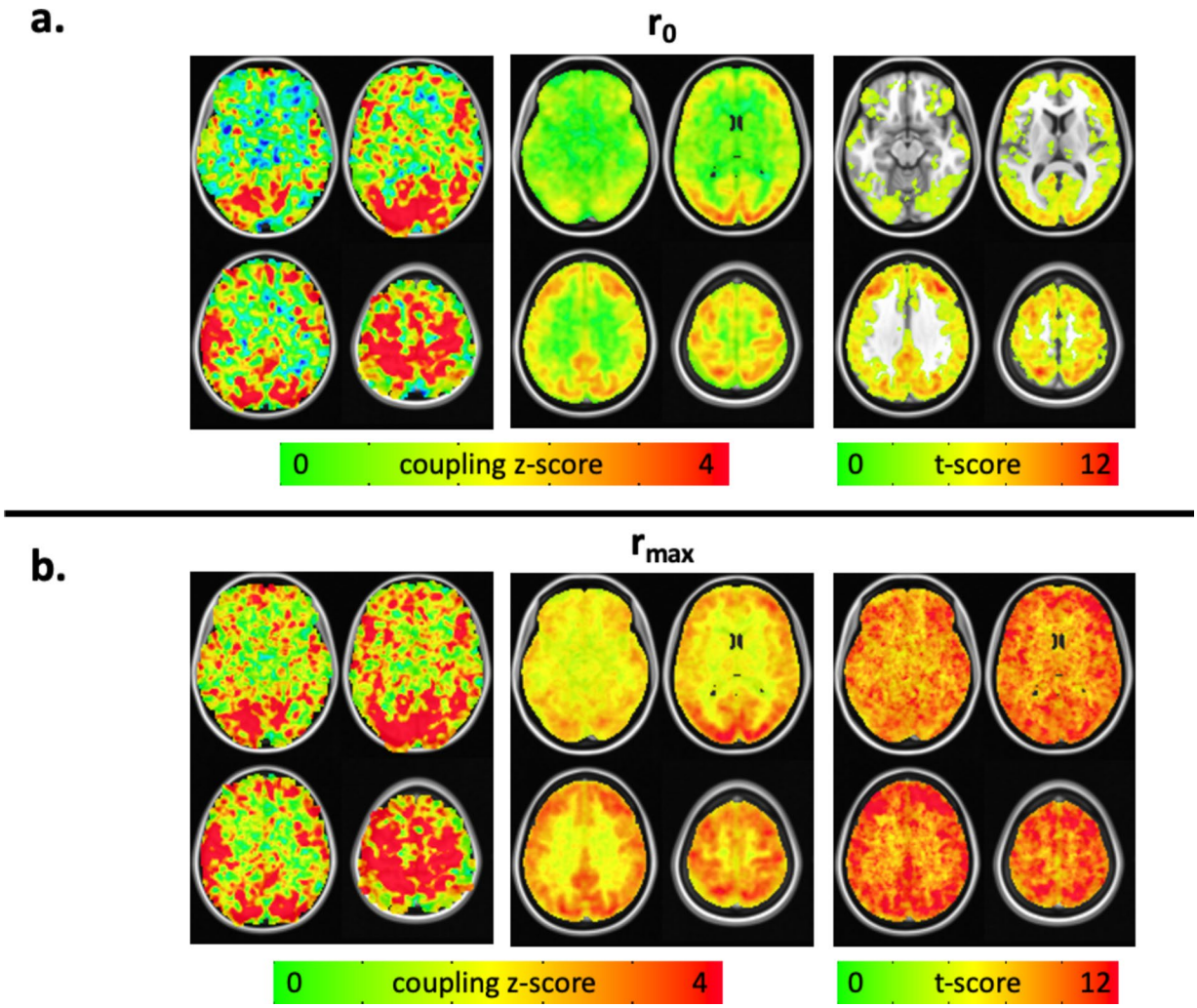

Fig. 2. Group maps of BOLD-CBF Coupling. Representative individual subject maps of r_0 (**a**) and r_{max} (**b**) are shown on the left. Group average maps of r_0 and r_{max} are shown in the middle, and one sample t-test results are shown on the right. Higher coupling was observed in the visual cortex, parietal areas, frontal regions, and motor cortices for r_0 and r_{max}. Coupling was more widespread for r_{max}. One sample t-test results for maps of r_0 and r_{max} were thresholded at $t > 4$. For both metrics nearly the entire gray matter was significant with the exception of the temporal lobe and orbitofrontal cortex for r_0.

and r_0 regions of the temporal cortex, subcortex, and OFC are showed lower coupling compared to the rest of the gray matter (Fig. 2). Significant coupling was present throughout nearly all gray matter for r_{max} and all gray matter, except for regions of the temporal cortex and the orbitofrontal cortex (OFC), which typically exhibit reduced data quality (tSNR) and signal dropouts, for r_0.

Despite this, the group averages showed stronger coupling in similar areas as the above studies including default mode and visual networks and frontal areas. As shown in Fig. 5, the mean coupling values for the Yeo networks varied between 0.2 and 0.25 for r_{max}, and between 0.1 and 0.15 for r_0, except for the limbic network (Yeo 5) which exhibited lower coupling values, particularly for r_0. These values are lower than the coupling value of 0.32 reported in[13]. Notably, the values in Chiacchiaretta et al. were only extracted from significant areas which may explain the higher value.

In order to tease apart the relationship between BOLD-CBF coupling and traditional RS metrics including mReHo and mALFF we performed a correlation analysis. Here, the BOLD and PW timeseries were correlated on a voxelwise basis to extract dynamic coupling measures, as opposed to static CBF measures in the above studies. Overall, similar correlation patterns were seen between r_0 and r_{max} and the traditional RS metrics mALFF and mReHo (see Figs. 3 and 6). Significant correlation corresponded to areas of heightened coupling, including visual, parietal, motor, and frontal areas. These results indicate BOLD-CBF coupling can provide similar, but complimentary measures to traditional NVC-sensitive RS metrics.

The question remains as to the physiological relevance of BOLD-CBF coupling and its relationship to resting state BOLD metrics. Champagne et al. compared BOLD-CBF coupling between young and old participants finding lower coupling in older participants[49]. Furthermore, they found coupling accounted for significant variability in RSFC strength between young and old participants mitigating the connectivity differences between

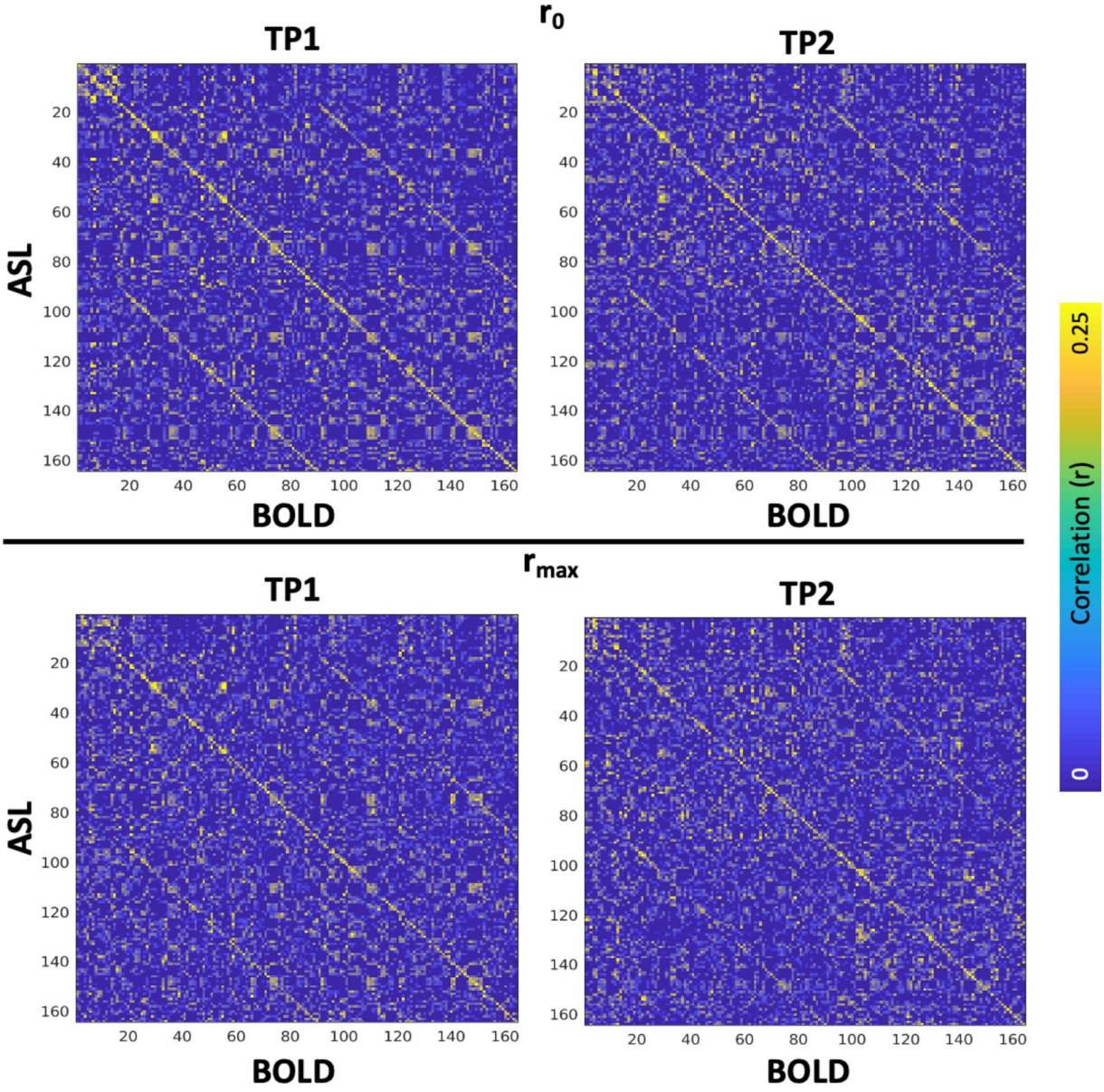

Fig. 3. ROI-based BOLD-CBF coupling matrices for r_0 (top) and r_{max} (bottom). A prominent diagonal line of high correlation is present for all matrices, indicating correlation is higher between BOLD and PW timeseries for the same ROI compared to other ROIs. Secondary diagonals are observed in the bottom left and top right quadrants corresponding to the correlation between BOLD and PW timeseries in contralateral ROIs.

the groups[49]. Thus, differences in connectivity between age groups could be due to vascular factors, which may need to be considered when interpreting BOLD measurements. They suggest changes in vessel stiffness with aging could drive changes in synchronicity between BOLD and CBF time series, compromising the neurovascular unit. Another study looked at changes in BOLD-CBF coupling with age, also finding lower coupling in older subjects[13]. BOLD-CBF connectivity was also found to be positively correlated with RSFC strength in several common brain networks and inversely correlated with macrovascular volume fraction suggesting BOLD-CBF coupling is a central factor influencing connectivity strength. The BOLD/perfusion ratio was also found to be higher during a metabolically demanding visual checkerboard task compared to less metabolically demanding resting state and breath holding (BH) tasks. Our MBME BOLD/ASL sequence provides increased temporal resolution and sensitivity as evidenced by widespread BOLD-CBF coupling throughout gray matter. Thus, it shows the potential to evaluate more subtle aspects of the relationship between CBF and BOLD both in the resting state and during tasks, and more accurately relate this coupling to physiological factors. Furthermore, our findings of positive correlations between mALFF and mReHo and BOLD-CBF coupling support the idea that BOLD-CBF coupling is related to brain connectivity.

A subset of subjects also returned for repeat scans allowing reproducibility and reliability metrics to be calculated. In general, reproducibility was higher for the traditional RS metrics compared to BOLD-CBF coupling

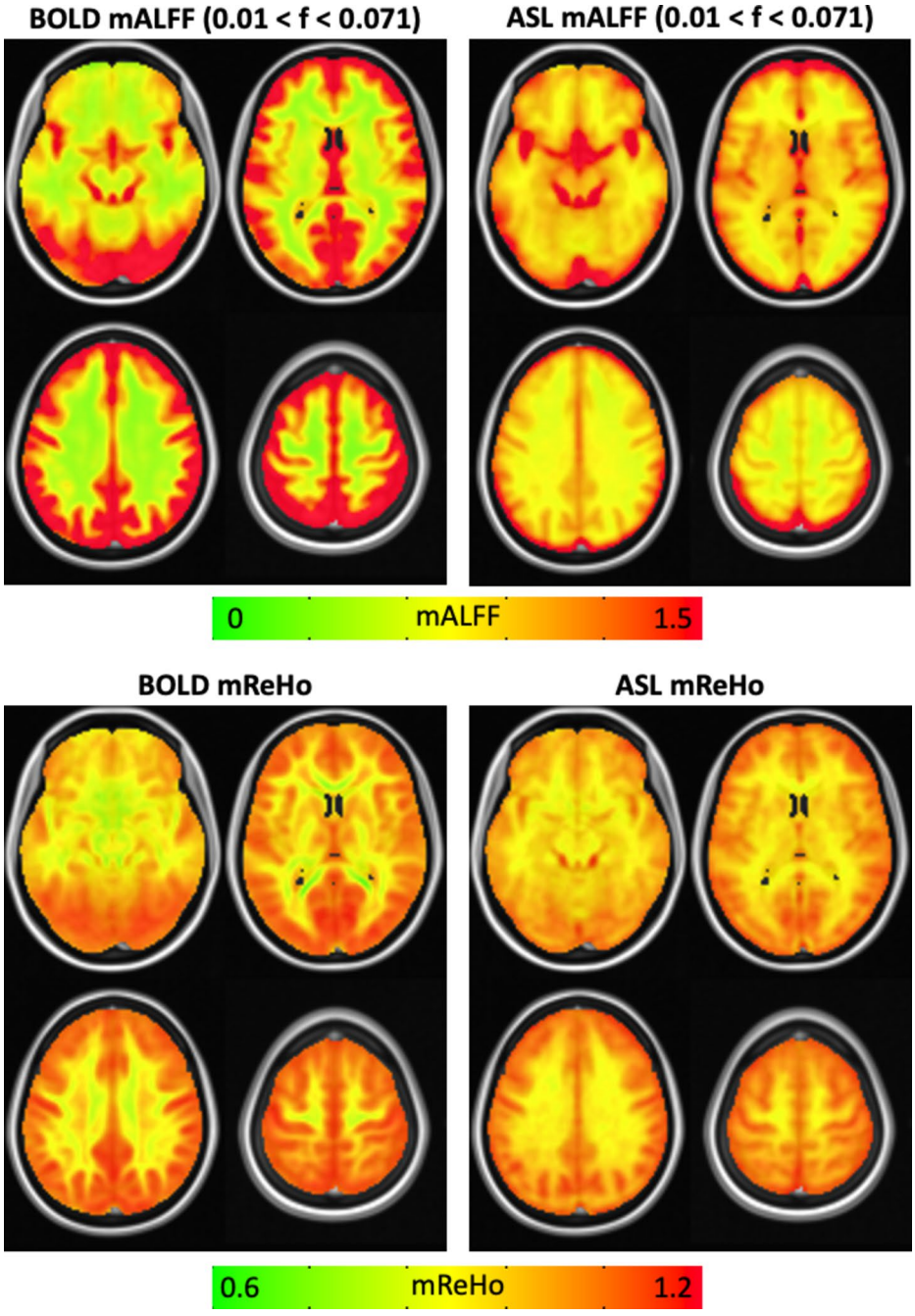

Fig. 4. Group averaged resting state metrics including mALFF (top) and mReHo (bottom).

metrics. This makes sense as tSNR is much higher for BOLD data compared to CBF data. For coupling metrics, reproducibility was higher and wSD and bSD lower for r_{max} compared to r_0 despite lower overall correlation for r_0.

Reliability was assessed using voxelwise ICC(2,1). ICC was high for BOLD RS metrics. ALFF was the most reliable with the majority of voxels having ICC > 0.8. ICC was low for the coupling metrics with ICC higher in areas with heightened coupling (i.e. visual and motor cortices). Along the same lines, wSD was comparable and in many cases higher than bSD for the coupling and BOLD metrics indicating they are just as variable in the same subject over time compared to across subjects Thus, care must be taken incorporating longitudinal coupling results outside of these regions.

Finally, an ROI analysis was conducted where the BOLD signal in each of the 164 Freesurfer-derived gray matter and subcortical ROIs was correlated with PW signal from each ROI. This resulted in a 164 × 164 correlation matrix. As expected, these matrices consist of a prominent diagonal line showing that the BOLD timeseries is more similar to the ASL time series from the same ROI compared to the other ROIs. This is true across scan sessions and for both r_{max} and r_0. This lends further credence to the idea that the BOLD-CBF coupling is not

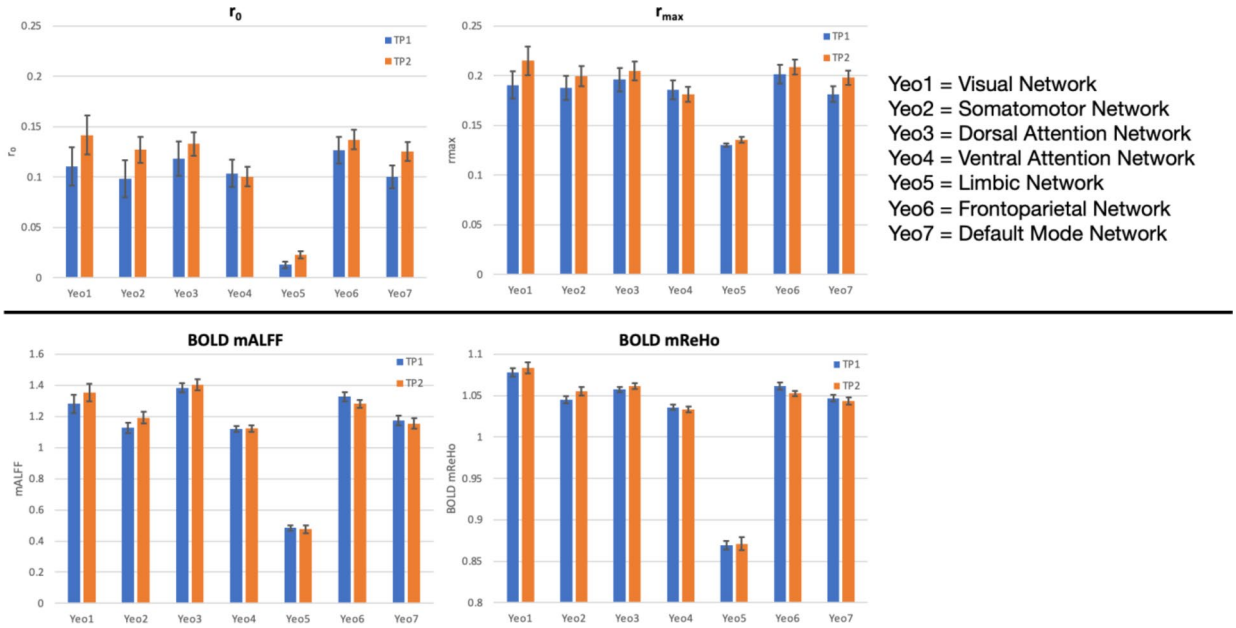

Fig. 5. Quantitative results for BOLD-CBF coupling metrics (top) and BOLD RS metrics (bottom). Mean values were extracted from 7 Yeo functional networks. There were no significant differences between TP1 and TP2 for any metric or ROI. Yeo5, corresponding to the limbic system had the lowest values for all metrics. Yeo1 = Visual; Yeo2 = Somatomotor; Yeo3 = Dorsal Attention; Yeo4 = Ventral Attention; Yeo5 = Limbic; Yeo6 = Frontoparietal; Yeo7 = Default Mode.

random. There are also two additional diagonal lines in lower left and upper right quadrants corresponding to the correlation between BOLD signal in the one ROI and PW signal in the contralateral ROI (and vice versa). Thus, the BOLD-CBF synchronization extends across hemispheres.

This study has some limitations. First, only healthy controls were used with a relatively narrow adult age range. It would be interesting to see the effects of disease and/or aging on BOLD-CBF coupling and correlation between BOLD-CBF coupling and traditional RS metrics. In addition, there was a large sampling bias towards females (19 F, 9 M). Also, we were only able to compute intersession reproducibility and reliability. Future studies could look at the intrasession reproducibility of these metrics. Also, because of the long TR, we did not compute fALFF, another common RSFC metric which measures the fraction of power in low frequencies compared to the entire frequency band. The Nyquist frequency for this dataset was 0.143 leading to very large fALFF values with little variability using typical bandpass freqencies. One potential factor in the interpretation of these results is the impact of CBV. The Davis model indicates BOLD and ASL signal are affected by CBV[16]. Thus, BOLD-ASL correlation, including parameters such as r_{max} and r_0, is also likely to be influenced by CBV. This also may be true for the correlation between ALFF and BOLD-ASL coupling as ALFF has been shown to explained by CBV variations[50]. While CBV changes may play a role, direct CBV measurement was beyond the scope of our current study. A PLD of 1000ms was chosen for this study as a trade-off between spatial accuracy and TR while also trying to avoid intravascular artifacts, characterized by hyperintense signal in large vessels on the perfusion-weighted image associated with long arterial transit times. This could be further amplified by the interleaved MB slice acquisition where superior slices are acquired earlier in the readout. Previous studies have used these parameters to estimate ASL and BOLD resting state networks[28], showing that ASL resting state networks can be reliably detected. We also observed banding artifacts in the perfusion-weighted images due to different PLDs at different slice levels. No processing corrections were performed aside from spatial smoothing. Finally, care must be taken when interpreting BOLD-CBF coupling as neurovascular coupling as the two are related, but not identical.

Conclusion

In conclusion, heightened BOLD-CBF coupling was found in major brain networks. BOLD-CBF coupling was also significantly correlated with traditional RS metrics including mReHo and mALFF in major network hubs indicating coupling may provide complimentary NVC-sensitive measures.

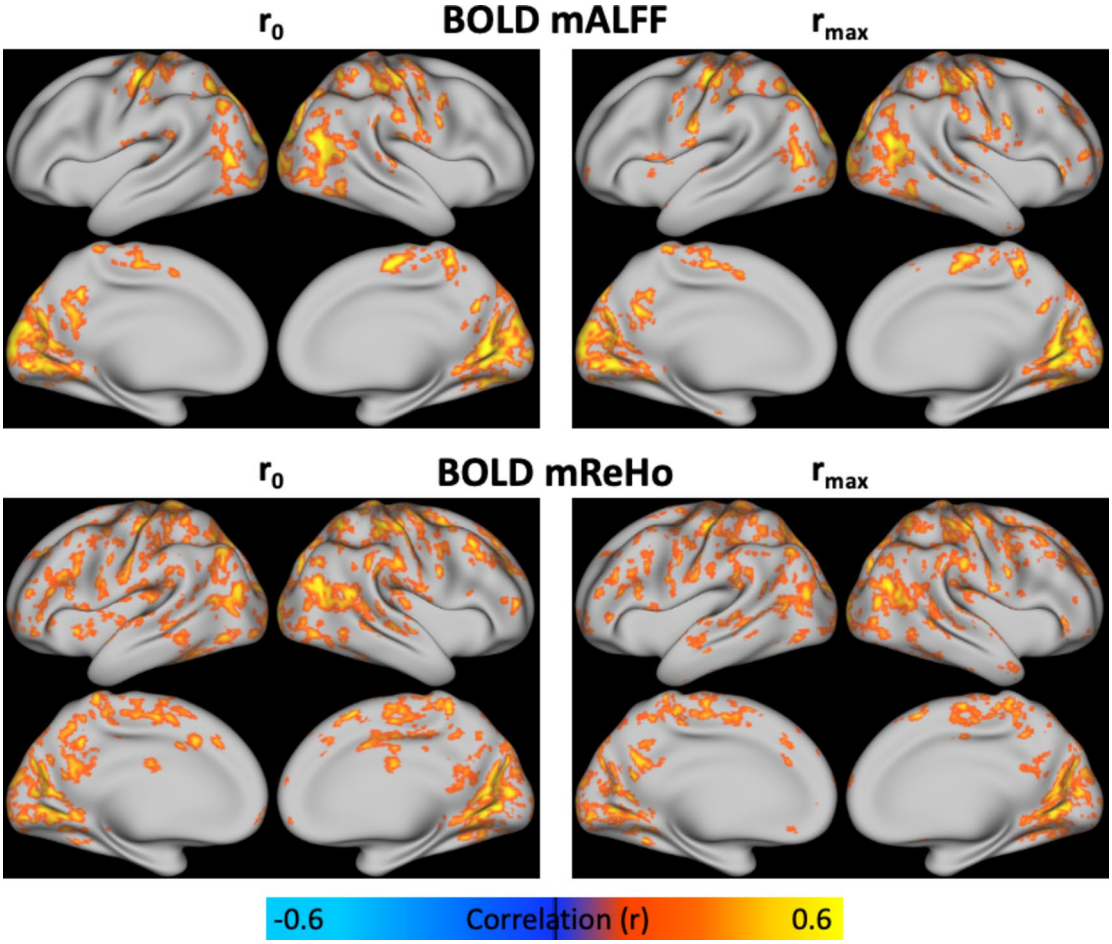

Fig. 6. Correlation between BOLD RS metrics and BOLD-CBF coupling metrics. Results for r_0 and r_{max} were similar for all RS metrics. Significant correlation between coupling and RS metrics was seen mainly in the visual cortex and motor cortex with significant correlation also seen in parietal and frontal areas.

	r_0			r_{max}		
ROI	wSD	bSD	Rep	wSD	bSD	Rep
Visual	0.053	0.076	0.732	0.036	0.057	0.892
Somatomotor	0.053	0.059	0.741	0.032	0.044	0.912
Dorsal attention	0.040	0.058	0.845	0.031	0.041	0.929
Ventral attention	0.036	0.045	0.809	0.026	0.032	0.923
Limbic	0.016	0.010	0.052	0.010	0.008	0.955
Frontoparietal	0.044	0.038	0.824	0.032	0.029	0.916
Default	0.043	0.035	0.759	0.026	0.028	0.918

Table 1. BOLD-CBF Coupling Metric variability. *wSD* within subject standard deviation, *bSD* between subject standard deviation, *Rep* reproducibility.

ROI	ASL mReHo			BOLD mReHo			ASL mALFF			BOLD mALFF		
	wSD	bSD	Rep	wSD	bSD	Rep	wSD	bSD	Rep	wSD	bSD	Rep
Visual	0.014	0.015	0.992	0.014	0.024	0.993	0.047	0.076	0.974	0.139	0.232	0.945
Somatomotor	0.012	0.013	0.993	0.018	0.017	0.991	0.025	0.030	0.984	0.089	0.142	0.959
Dorsal attention	0.010	0.007	0.995	0.014	0.011	0.993	0.027	0.046	0.983	0.076	0.132	0.968
Ventral attention	0.012	0.009	0.994	0.012	0.012	0.993	0.033	0.036	0.982	0.059	0.077	0.972
Limbic	0.011	0.017	0.993	0.026	0.022	0.983	0.035	0.070	0.976	0.047	0.082	0.940
Frontoparietal	0.010	0.010	0.994	0.013	0.015	0.994	0.028	0.049	0.983	0.077	0.106	0.962
Default	0.005	0.008	0.997	0.013	0.016	0.993	0.026	0.044	0.985	0.075	0.129	0.963

Table 2. Traditional RS metric variability. *wSD* within subject standard deviation, *bSD* between subject standard deviation, *Rep* reproducibility.

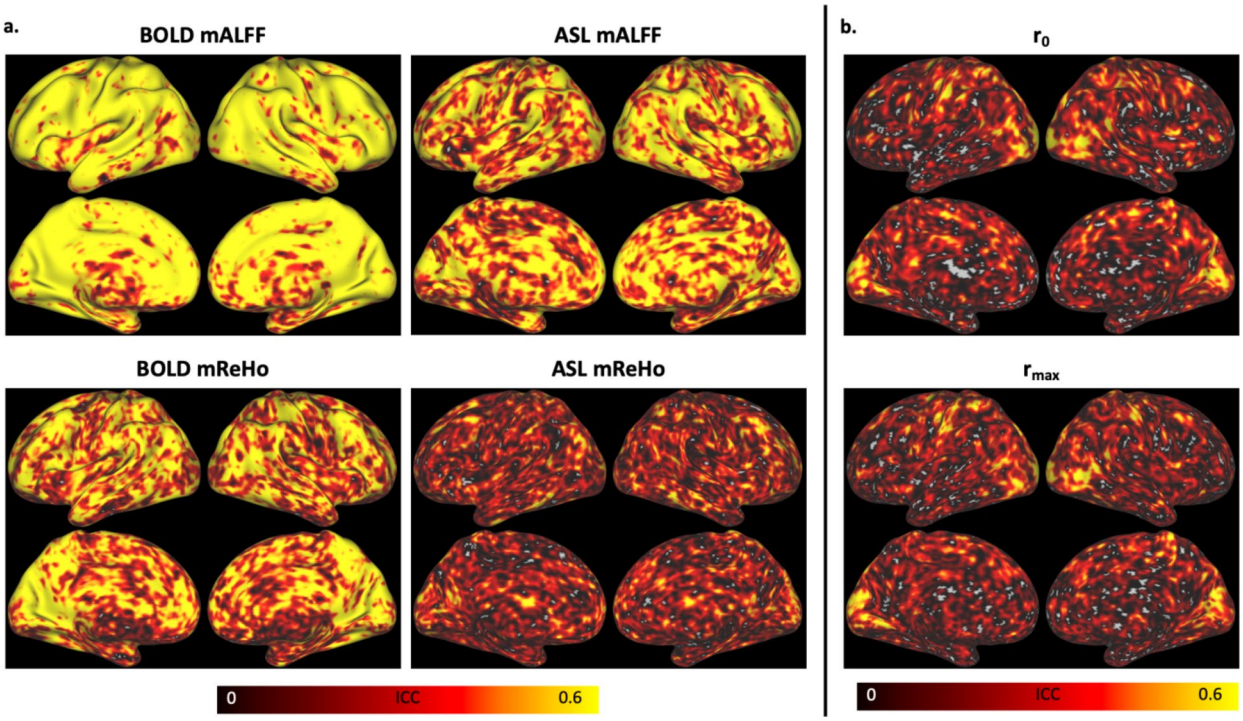

Fig. 7. ICC for RS metrics (**a**) and BOLD-CBF coupling metrics (**b**). ICC was higher for the RS metrics compared to coupling metrics. ICC was low for the coupling metrics; however, areas of heightened ICC were seen in the visual and motor cortices. These areas corresponded to areas of higher correlation between coupling metrics and RS metrics.

Data availability

Data is available on request from Yang Wang at yangwang@mcw.edu.

Received: 22 March 2024; Accepted: 26 November 2024
Published online: 15 January 2025

References

1. Iadecola, C. The neurovascular unit coming of age: a journey through neurovascular coupling in health and disease. *Neuron* **96**, 17–42 (2017).
2. Phillips, A. A., Chan, F. H., Zheng, M. M., Krassioukov, A. V. & Ainslie, P. N. Neurovascular coupling in humans: physiology, methodological advances and clinical implications. *J. Cereb. Blood flow. Metab. Off. J. Int. Soc. Cereb. Blood Flow Metab.* **36**, 647–664. https://doi.org/10.1177/0271678x15617954 (2016).
3. Ogawa, S., Lee, T. M., Kay, A. R. & Tank, D. W. Brain magnetic resonance imaging with contrast dependent on blood oxygenation. *Proc. Natl. Acad. Sci. U. S. A.* **87**, 9868–9872. https://doi.org/10.1073/pnas.87.24.9868 (1990).
4. Tarantini, S., Tran, C. H. T., Gordon, G. R., Ungvari, Z. & Csiszar, A. Impaired neurovascular coupling in aging and Alzheimer's disease: contribution of astrocyte dysfunction and endothelial impairment to cognitive decline. *Exp. Gerontol.* **94**, 52–58. https://doi.org/10.1016/j.exger.2016.11.004 (2017).
5. Kisler, K., Nelson, A. R., Montagne, A. & Zlokovic, B. V. Cerebral blood flow regulation and neurovascular dysfunction in Alzheimer disease. *Nat. Rev. Neurosci.* **18**, 419–434. https://doi.org/10.1038/nrn.2017.48 (2017).

6. Snyder, H. M. et al. Vascular contributions to cognitive impairment and dementia including Alzheimer's disease. *Alzheimers Dement.* **11**, 710–717. https://doi.org/10.1016/j.jalz.2014.10.008 (2015).
7. Zlokovic, B. V. Neurovascular mechanisms of Alzheimer's neurodegeneration. *Trends Neurosci.* **28**, 202–208. https://doi.org/10.1016/j.tins.2005.02.001 (2005).
8. Ghariq, E., Chappell, M. A., Schmid, S., Teeuwisse, W. M. & van Osch, M. J. P. Effects of background suppression on the sensitivity of dual-echo arterial spin labeling MRI for BOLD and CBF signal changes. *NeuroImage* **103**, 316–322. https://doi.org/10.1016/j.neuroimage.2014.09.051 (2014).
9. Schmithorst, V. J. et al. Optimized simultaneous ASL and BOLD functional imaging of the whole brain. *J. Magn. Reson. Imaging JMRI* **39**, 1104–1117. https://doi.org/10.1002/jmri.24273 (2014).
10. Tak, S., Polimeni, J. R., Wang, D. J., Yan, L. & Chen, J. J. Associations of resting-state fMRI functional connectivity with Flow-BOLDcoupling and regional vasculature. *Brain Connect.* **5**, 137–146. https://doi.org/10.1089/brain.2014.0299 (2015).
11. Tak, S., Wang, D. J. J., Polimeni, J. R., Yan, L. & Chen, J. J. Dynamic and static contributions of the cerebrovasculature to the resting-state BOLD signal. *NeuroImage* **84**, 672–680. https://doi.org/10.1016/j.neuroimage.2013.09.057 (2014).
12. Zhu, S., Fang, Z., Hu, S., Wang, Z. & Rao, H. Resting state brain function analysis using concurrent BOLD in ASL perfusion fMRI. *PloS One* **8**, e65884. https://doi.org/10.1371/journal.pone.0065884 (2013).
13. Chiacchiaretta, P., Cerritelli, F., Bubbico, G., Perrucci, M. G. & Ferretti, A. Reduced dynamic coupling between spontaneous BOLD-CBF fluctuations in older adults: a dual-Echo pCASL Study. *Front. Aging Neurosci.* **10**, 115. https://doi.org/10.3389/fnagi.2018.00115 (2018).
14. Cohen, A. D., Nencka, A. S. & Wang, Y. Multiband multi-echo simultaneous ASL/BOLD for task-induced functional MRI. *PloS One* **13**, e0190427. https://doi.org/10.1371/journal.pone.0190427 (2018).
15. Champagne, A. A. et al. The physiological basis underlying functional connectivity differences in older adults: a multi-modal analysis of resting-state fMRI. *Brain Imaging Behav.* **16**, 1575–1591 (2022).
16. Davis, T. L., Kwong, K. K., Weisskoff, R. M. & Rosen, B. R. Calibrated functional MRI: mapping the dynamics of oxidative metabolism. *Proc. Natl. Acad. Sci.* **95**, 1834–1839 (1998).
17. Yu-Feng, Z. et al. Altered baseline brain activity in children with ADHD revealed by resting-state functional MRI. *Brain Dev.* **29**, 83–91 (2007).
18. Cordes, D. et al. Frequencies contributing to functional connectivity in the cerebral cortex in resting-state data. *Am. J. Neuroradiol.* **22**, 1326–1333 (2001).
19. Di, X. et al. The influence of the amplitude of low-frequency fluctuations on resting-state functional connectivity. *Front. Hum. Neurosci.* **7**, 118 (2013).
20. Yang, H. et al. Amplitude of low frequency fluctuation within visual areas revealed by resting-state functional MRI. *Neuroimage* **36**, 144–152 (2007).
21. Baller, E. B. et al. Developmental coupling of cerebral blood flow and fMRI fluctuations in youth. *Cell Rep.* **38** (2022).
22. Jiang, L. & Zuo, X. N. Regional homogeneity: a multimodal, multiscale neuroimaging marker of the human connectome. *Neuroscientist* **22**, 486–505 (2016).
23. Zang, Y., Jiang, T., Lu, Y., He, Y. & Tian, L. Regional homogeneity approach to fMRI data analysis. *Neuroimage* **22**, 394–400 (2004).
24. Yuan, R. et al. Regional homogeneity of resting-state fMRI contributes to both neurovascular and task activation variations. *Magn. Reson. Imaging* **31**, 1492–1500 (2013).
25. Guo, X. et al. Altered neurovascular coupling in neuromyelitis optica. *Hum. Brain Mapp.* **40**, 976–986 (2019).
26. Liu, X. et al. Altered neurovascular coupling in subcortical ischemic vascular disease. *Front. Aging Neurosci.* **13**, 598365 (2021).
27. Liao, D. et al. Alterations in regional homogeneity and functional connectivity associated with cognitive impairment in patients with hypertension: a resting-state functional magnetic resonance imaging study. *Hypertens. Res.* **46**, 1311–1325 (2023).
28. Cohen, A. D., Nencka, A. S., Lebel, R. M. & Wang, Y. Multiband multi-echo imaging of simultaneous oxygenation and flow timeseries for resting state connectivity. *PloS One* **12**, e0169253. https://doi.org/10.1371/journal.pone.0169253 (2017).
29. Amemiya, S., Yamashita, H., Takao, H. & Abe, O. Integrated multi-echo denoising strategy improves identification of inherent language laterality. *Magn. Reson. Med.* **81**, 3262–3271 (2019).
30. Kundu, P. et al. Multi-echo fMRI: a review of applications in fMRI denoising and analysis of BOLD signals. *Neuroimage* **154**, 59–80 (2017).
31. Lynch, C. J. et al. Rapid precision functional mapping of individuals using multi-echo fMRI. *Cell Rep.* 33 (2020).
32. Evans, J. W., Kundu, P., Horovitz, S. G. & Bandettini, P. A. Separating slow BOLD from non-BOLD baseline drifts using multi-echo fMRI. *NeuroImage* **105**, 189–197. https://doi.org/10.1016/j.neuroimage.2014.10.051 (2015). https://doi.org/http://dx.doi.org/
33. Gonzalez-Castillo, J. et al. Evaluation of multi-echo ICA denoising for task based fMRI studies: Block designs, rapid event-related designs, and cardiac-gated fMRI. *Neuroimage* **141**, 452–468. https://doi.org/10.1016/j.neuroimage.2016.07.049 (2016).
34. Kundu, P. et al. Integrated strategy for improving functional connectivity mapping using multiecho fMRI. *Proc. Natl. Acad. Sci. U. S. A.* **110**, 16187–16192. https://doi.org/10.1073/pnas.1301725110 (2013).
35. Kundu, P., Inati, S. J., Evans, J. W., Luh, W. M. & Bandettini, P. A. Differentiating BOLD and non-BOLD signals in fMRI time series using multi-echo EPI. *Neuroimage* **60**, 1759–1770. https://doi.org/10.1016/j.neuroimage.2011.12.028 (2012).
36. Moia, S. et al. ICA-based denoising strategies in breath-hold induced cerebrovascular reactivity mapping with multi echo BOLD fMRI. *Neuroimage* **233**, 117914 (2021).
37. Fischl, B. FreeSurfer. *Neuroimage* **62**, 774–781 https://doi.org/10.1016/j.neuroimage.2012.01.021 (2012).
38. Cox, R. W. AFNI: software for analysis and visualization of functional magnetic resonance neuroimages. *Comput. Biomed. Res.* **29**, 162–173. https://doi.org/10.1006/cbmr.1996.0014 (1996).
39. Cox, R. W. AFNI: what a long strange trip it's been. *Neuroimage* **62**, 743–747. https://doi.org/10.1016/j.neuroimage.2011.08.056 (2012).
40. Jenkinson, M., Beckmann, C. F., Behrens, T. E., Woolrich, M. W. & Smith, S. M. Fsl. *Neuroimage* **62**, 782–790 https://doi.org/10.1016/j.neuroimage.2011.09.015 (2012).
41. Glasser, M. F. et al. The minimal preprocessing pipelines for the Human Connectome Project. *NeuroImage* 80, 105–124 https://doi.org/http://dx.doi.org/ (2013). https://doi.org/10.1016/j.neuroimage.2013.04.127
42. Jenkinson, M., Bannister, P., Brady, M. & Smith, S. Improved optimization for the robust and accurate linear registration and motion correction of brain images. *Neuroimage* **17**, 825–841. https://doi.org/10.1016/s1053-8119(02)91132-8 (2002).
43. Posse, S. et al. Enhancement of BOLD-contrast sensitivity by single-shot multi-echo functional MR imaging. *Magn. Reson. Med.* **42**, 87–97 (1999).
44. Li, Y. O., Adalı, T. & Calhoun, V. D. Estimating the number of independent components for functional magnetic resonance imaging data. *Hum. Brain Mapp.* **28**, 1251–1266 (2007).
45. Chuang, K. H. et al. Mapping resting-state functional connectivity using perfusion MRI. *Neuroimage* **40**, 1595–1605. https://doi.org/10.1016/j.neuroimage.2008.01.006 (2008).
46. Yeo, B. T. et al. The organization of the human cerebral cortex estimated by intrinsic functional connectivity. *J. Neurophysiol.* **106**, 1125–1165. https://doi.org/10.1152/jn.00338.2011 (2011).
47. Cohen, A. D., Tomasi, D., Shokri-Kojori, E., Nencka, A. S. & Wang, Y. Functional connectivity density mapping: comparing multiband and conventional EPI protocols. *Brain Imaging Behav.* **12**, 848–859 (2018).
48. Tomasi, D., Shokri-Kojori, E. & Volkow, N. Temporal changes in local functional connectivity density reflect the temporal variability of the amplitude of low frequency fluctuations in gray matter. *PloS One* **11**, e0154407 (2016).

49. Champagne, A. A. et al. Multi-modal normalization of resting-state using local physiology reduces changes in functional connectivity patterns observed in mTBI patients. *NeuroImage Clin.* **26**, 102204 (2020).
50. Deng, S. et al. Hemodynamic and metabolic correspondence of resting-state voxel-based physiological metrics in healthy adults. *Neuroimage* **250**, 118923 (2022).

Acknowledgements
This work was funded by a research grant from GE Healthcare to Yang Wang.

Author contributions
A.C.: Conceptualization, Methodology, Software, Investigation, Formal analysis, Visualization, Writing – original draft, Writing – review & editing. S.M.: Conceptualization, Writing – review & editing. G.B.P.: Conceptualization, Writing – review & editing. C.C.G.: Conceptualization, Writing – review & editing. Y.W.: Conceptualization, Resources, Methodology, Investi-gation, Formal analysis, Writing – review & editing, Supervision, Funding Acquisition.

Declarations

Competing interests
The authors declare no competing interests.

Additional information
Correspondence and requests for materials should be addressed to A.D.C.

Reprints and permissions information is available at www.nature.com/reprints.

Publisher's note Springer Nature remains neutral with regard to jurisdictional claims in published maps and institutional affiliations.